How to cite: *Angew. Chem. Int. Ed.* **2021**, *60*, 18448–18453
International Edition: doi.org/10.1002/anie.202104183
German Edition: doi.org/10.1002/ange.202104183

Battery Materials

Double Ionic–Electronic Transfer Interface Layers for All-Solid-State Lithium Batteries

Jingang Zheng, Chengguo Sun, Zhenxing Wang, Shaojun Liu, Baigang An, Zhenhua Sun, and Feng Li**

Abstract: *Large-scale implementation of all-solid-state lithium batteries is impeded by the physical limitations of the interface between the electrode and solid electrolyte; specifically, high resistance and poor stability, as well as poor compatibility with Li^+ migration. We report double ionic–electronic transfer interface layers grown at electrode–electrolyte interfaces by in situ polymerization of 2,2′-bithiophene in polyethylene oxide (PEO) electrolyte. For all-solid-state $LiFePO_4$ ‖ PT-PEO-PT ‖ Li cells, the formation of a conductive polythiophene (PT) layer at the cathode–electrolyte interface resulted in an at least sevenfold decrease in interface resistance, and realized a capacity retention of about 94 % after 1000 cycles along with a lower polarization voltage under a rate of 2 C. The mixed ionic–electronic conductive layers imparted superior interface stability and contact while keeping good compatibility with the Li anode.*

With the wide use of lithium-ion batteries (LIBs), liquid electrolytes have aroused major concerns about safety issues due to the flammability of liquid organic solvent, and hazards of electrolyte leakage.[1] Solid polymer electrolytes (SPEs) have been considered as an optimum solution to achieve the safe and high-energy-density LIBs.[2] While various SPEs have addressed the safety and performance considerations, several constraints, such as high interfacial resistance, poor compatibility and unstable solid-electrolyte interphase formation, have hindered their widespread application in all-solid-state LIBs.[3] Several approaches to solve the solid-state electrolyte-electrode interface issues were proposed, including interface softening,[4] electrodes coating or pulsed laser deposition,[5] buffer layer construction[6] and constructing multifunctional solid electrolyte interface.[7] The progress has been made in improving the interface of solid-solid phase. However, the stable and compatible interfacial layers, and low contact resistance between SPEs and electrodes are much desired.

Generally, SPEs feature good interfacial adhesion to electrodes. However, high interfacial resistance between electrode and SPE is considered to be the most challenging for the application of all-solid-state LIBs. In fact, upon cycling, the poor chemical stability between the electrode and SPEs can lead to the formation of the interfacial passivation layer, which results in high resistance, high polarization and short cycle life.[8] To address these issues, three major aspects need to be considered towards building favorable solid-solid interface layers in polymer electrolyte-based LIB: (1) low interfacial resistance, especially for overcoming the charge-transfer resistance barrier, which is closely associated with the kinetics of the electrochemical reaction;[9] (2) stable chemical compatibility of the electrode–electrolyte interface to withstand the interface deterioration after long-term cycling; (3) robust ionic transfer layer beneficial for Li^+ transport across the interface. Considerations for incorporating these requirements into SPEs, the key is to reduce interfacial resistance and keep the interface stable simultaneously while increasing the Li^+ transfer sites at the interface. One effective idea similar to the solid electrolyte interface (SEI) formed in liquid electrolyte is in situ fabrication of interface layer from the raw solid electrolyte. When the interface layers grow from the polymer electrolyte, the solid-solid contact appears well-connected, and small charge transfer resistance is expected.[10]

Herein, we reported in situ electrochemical polymerization method to produce double conductive polythiophene (PT) layers that are principally formed at cathode–electrolyte interface and little either formed at anode–electrolyte interface. The mixed ionic–electronic transfer interface layer consisting of PT and PEO can reduce the contact resistance significantly and improve interface stability against the electrochemical oxidation decomposition. More importantly, the in situ growth of the mixed ionic–electronic transfer layer at the electrode–electrolyte interface facilitate Li^+ migration, but achieve good compatibility with Li anode. When combined Li anode with lithium iron phosphate ($LiFePO_4$) or high voltage $LiNi_{0.5}Co_{0.2}Mn_{0.3}O_2$ (NCM523) cathode, the all-solid-state cell with the mixed ionic–electronic transfer layers on both electrode–electrolyte interfaces enable high-rate capability and stable long-term performance with low polarization.

Figure 1a illustrates the strategy for formation of the mixed ionic–electronic transfer layer from the solid-state PEO electrolyte. The 2,2′-bithiophene (BT) was used as

[*] J. Zheng, Prof. Dr. C. Sun, S. Liu, Prof. Dr. B. An
School of Chemical Engineering
University of Science and Technology Liaoning
Anshan 114051 (China)
E-mail: sunyangguo2004@163.com
Prof. Dr. C. Sun, Z. Wang, Prof. Dr. Z. Sun, Prof. Dr. F. Li
Shenyang National Laboratory for Materials Science
Institute of Metal Research, Chinese Academy of Science
Shenyang 110016 (China)
E-mail: fli@imr.ac.cn
Prof. Dr. C. Sun
School of Chemical Engineering
Nanjing University of Science and Technology
Nanjing 210094 (China)
Supporting information and the ORCID identification number(s) for the author(s) of this article can be found under: https://doi.org/10.1002/anie.202104183.

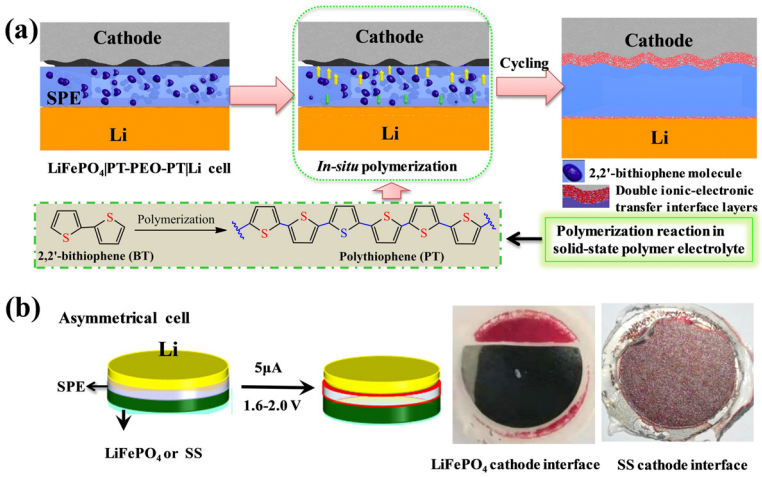

Figure 1. Creating the interface between electrode and electrolyte. a) The formation of a conductive interface layer in a $LiFePO_4$ || PT-PEO-PT || Li cell. b) The electrochemical polymerization method for cell configuration. After disassembling, the PT formed on the interface between $LiFePO_4$ or SS cathode and electrolyte. For the convenience of viewing the polythiophene, a small part of the $LiFePO_4$ electrode was cut off.

additive in PEO-based electrolyte solution, after removing the solvent, the obtained polymer electrolyte membranes were, respectively assembled into $LiFePO_4$ || PT-PEO-PT || Li, SS || PT-PEO-PT || Li (SS refers to stainless steel cathode) and Li || PT-PEO-PT || Li cells. To accelerate the polymerization of BT at the electrode–electrolyte interface, two electrochemical polymerization methods were performed at 60 °C. One method consists of cyclic voltammetry for the symmetrical cell configuration in which the cell is charged after 100 cycles with scan rate 2 mV s^{-1} while the voltage is scanned from 0 to 1.0 V and back to 0 V. The other involves galvanostatic polarization method controlled with galvanostatic charge-discharge instrument where the asymmetrical cell is discharged/charge for about 300 cycles at constant-current of 5 μA within the voltage range between 1.5 V and 2.0 V. During electrochemical cycling, the BT in PEO electrolyte membranes principally migrated towards cathode interface, and the others moved toward the anode interface. The aggregated BT were easily polymerized to produce the PTs. The corresponding mechanism diagram is shown in Figure S1 (Supporting Information). To visualize the formed PT at interface layer, both $LiFePO_4$ || PT-PEO-PT || Li and SS || PT-PEO-PT || Li cells were allowed to treat with galvanostatic polarization, after which the cells were disassembled to analyze the interface layer. The magenta PT composite layer was produced between the cathode and electrolyte membranes (Figure 1 b).

Infrared spectroscopy was used to further confirm the formation of PT, the characteristic peaks are consistent with the electrochemical polymerization of thiophene onto carbon paper by similar galvanostatic method (Figure S2).[11] Optical microscope was also used to characterize the surface of the conductive interface layer close to electrolyte membrane, it can be found that the formed PTs present the morphology similar to the pomegranate seed-like structure adhered to electrolyte membrane (Figure 2 a; Figure S3), in which the core consists of seed-like granular with thick continuous shell. The low-magnification scanning electron microscope (SEM) image shows the PTs feature snowflake-like pattern (Figure S4), high-magnification SEM images show every "snowflake" consists of different particle types of varying shapes and sizes (Figure 2 b). To further view the formed PT layer on PEO-based electrolyte membrane, the SEM at low voltage mode (2 kV) has been used to observe the sample. Figure 2 c shows the PTs grew from the electrolyte membrane and the surface appears to coat with thin PEO tightly. After dissolving the whole electrolyte membrane in acetonitrile solution, the insoluble PTs were obtained by centrifugation, indicating the residual PTs are like sheet rather than particles (Figure S5), the rough surface shows multilayer structure that is composed of the aggregated flakes (Figure 2 d). The results demonstrate that the morphology and distribution of PTs growth were affected by PEO during electrochemical polymerization, and the strong intermolecular interaction between PEO chains and PTs makes them join together to form the mixed ionic–electronic transfer layer. The size distribution of PTs can fill the gap between cathode and electrolyte, which make the electrode–electrolyte interface well-connected. As further the observation was from the atomic force microscopy (AFM),

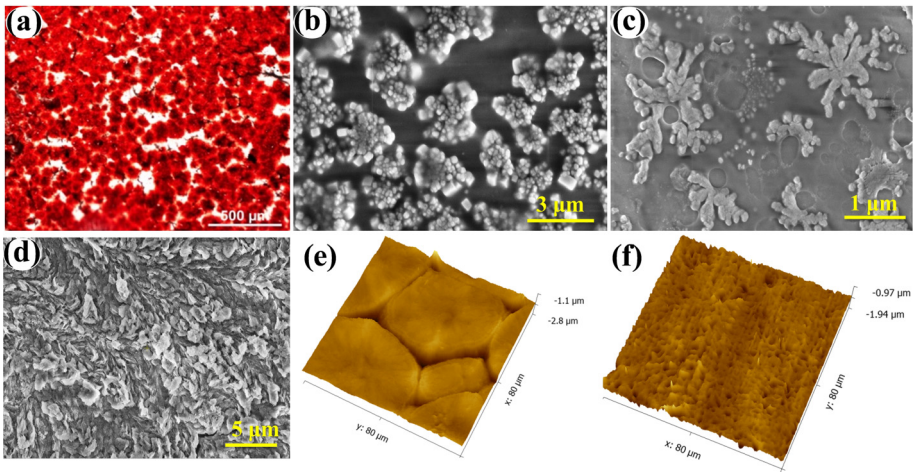

Figure 2. Morphology characterization. a) Optical microscope image of the surface of the electrolyte close to the cathode interface. b,c) SEM images of the surface of the electrolyte close to the cathode interface. d) SEM image of the polythiophene after removing the PEO. e) AFM image of the PEO electrolyte surface. f) AFM image of the surface of the electrolyte close to the cathode interface after polythiophene formation.

the pristine PEO membrane shows the presence of smooth surface and obvious crystalline phase boundary within the scanned area of 80×80 μm (Figure 2e). After the PTs formation, the AFM image reveals the rough surface topography (Figure 2f), at the selected area of 20×20 μm, the enlarged AFM image shows the rough and irregular holes (Figure S6), which closely matches the cathode surface consisting of $LiFePO_4$ particles with different sizes and shapes (Figure S7). The different sizes of PTs can make up the gap between electrode and electrolyte.

To gain further insights into the interfacial contact and the region where the PTs formed in $LiFePO_4$ || PT-PEO-PT || Li cell, the cross-sectional image of the electrode–electrolyte interface was investigated by SEM with energy dispersive X-ray spectrometry (EDS). In contrast to the $LiFePO_4$ || PEO interface (Figure 3a), the electrode–electrolyte interface of $LiFePO_4$ || PT-PEO-PT || Li cell displays good connection and compact contact without obvious boundary (Figure 3b). Figure 3c shows cross-sectional view of the $LiFePO_4$ || PT-PEO interface at higher magnification, and the corresponding sulfur element mapping measurement was taken to confirm the PT distribution, the sulfur is only detected in the area corresponding to the interfacial contact area (Figure 3d), indicative of the formation of PT occurred at the cathode–electrolyte interface. Figure 3e also presents the cross-sectional SEM-EDS images of the anode–electrolyte, good compatibility of Li anode–electrolyte interface was also achieved, however, the corresponding EDS images show the very weak signal of sulfur. When the polymer electrolyte membrane was peeled off from the Li metal anode, the thin uniform PT layer can be found on the Li foil (Figure 3f). The results demonstrate that the PTs principally formed at the cathode–electrolyte interface, while a small amount of PTs produced at the anode–electrolyte interface.

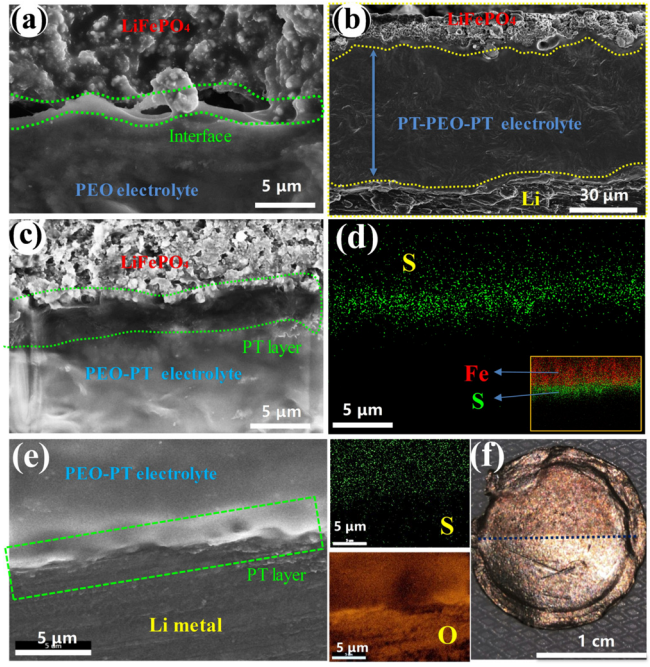

Figure 3. Cross-sectional SEM image of the electrode–electrolyte interface. a) SEM image of the PEO electrolyte-$LiFePO_4$ interface. b) SEM image of the two electrode–electrolyte interfaces in the $LiFePO_4$ || PT-PEO-PT || Li cell after cycling. c) SEM image of the PT-PEO electrolyte-$LiFePO_4$ interface. d) The corresponding S (Fe) element mapping of a cross-section of the PEO-PT electrolyte-$LiFePO_4$. e) SEM image of the PEO-PT electrolyte-Li metal interface and the corresponding element distributions at the interface. f) Digital photograph of the Li-metal interface disassembled from the cycled $LiFePO_4$ || PT-PEO-PT || Li cell. In sharp contrast, half of the $LiFePO_4$ electrode was used, which resulted in the formation of PT on the Li metal.

Electrochemical impedance spectrum (EIS) measurements before and after cycling was used to investigate the interface resistance by the conductive layers. Figure 4a shows the EIS of asymmetric SS || PT-PEO-PT || Li cell before cycling and after 300 cycles continuous galvanostatic polarization at the voltage from 1.5 to 2.0 V. The cell resistance remains at ≈3912 Ω before polarization, and then decreases to ≈360 Ω while keeping stable from 100 to 300 cycles. The results demonstrate after in situ polymerization, the PT has an obvious superiority in reducing the resistance and stabilizing the interface. Figure 4b shows the EIS of $LiFePO_4$ || PT-PEO-PT || Li cell after and before polarization, two semicircles locate in the high-frequency region and mid-frequency region represents the bulk resistance (R_b) of the solid electrolyte separator and interfacial resistance (R_i), respectively.[12] The growth of ionic–electronic transfer interface layer leads to significant reduction of R_i ranging from 13040 to 1765 Ω. As the cell continues to charge/discharge at 2 C rate between 2.5 and 4.2 V, the R_i decreases with the cycle number (Figure 4c), which relates to the consolidation of interface layers at elevated voltage. It is noteworthy that the double ionic–electronic transfer interface layer extended the electrochemical window up to about 4.9 V (Figure S8). For a better understanding of the reduced interface resistance caused by the electronic conductivity, the PT-bonded PEO membrane resistance was measured by chronopotentiometry based on the principle of four-point probe. After application of constant current (60 nA), the potential reaches a steady-state value over the time, and the membrane resistance varies directly with voltage (Figure 4d), a comparative analysis of voltage shows that the resistance of electrolyte membrane after the PTs formation, decreased by ≈70% as compared with that of the pristine PEO membrane. As a result of the low resistance and intimate contact interface, the PTs incorporated PEO membrane exhibits a high ionic conductivity of 1.06×10^{-4} S cm^{-1} and high Li^+ transference number of 0.54 at 40 °C, which is contrast to the pristine PEO with low ionic conductivity of 2.84×10^{-5} S cm^{-1} and Li^+ transference number of ≈0.28. (Figures S9–S11).

The lithium plating and stripping tests were carried out to evaluate the stability of the Li anode interface and the capability of Li^+ transport across the mixed ionic–electronic transfer layer. The Li || PT-PEO-PT || Li cell was first activated by cyclic voltammetry, and cycled under the current densities of 0.025, 0.05 and 0.1 mA cm^{-2} at 50 °C, respectively. As illustrated in Figure 4e, the intensity of voltage profile increases with the current density. At the current density of 0.1 mA cm^{-2}, the cell shows the overpotential less than 0.16 V. In contrast, the Li || PEO || Li cells shows the overpotential up to maximum 0.41 V even at low current density of

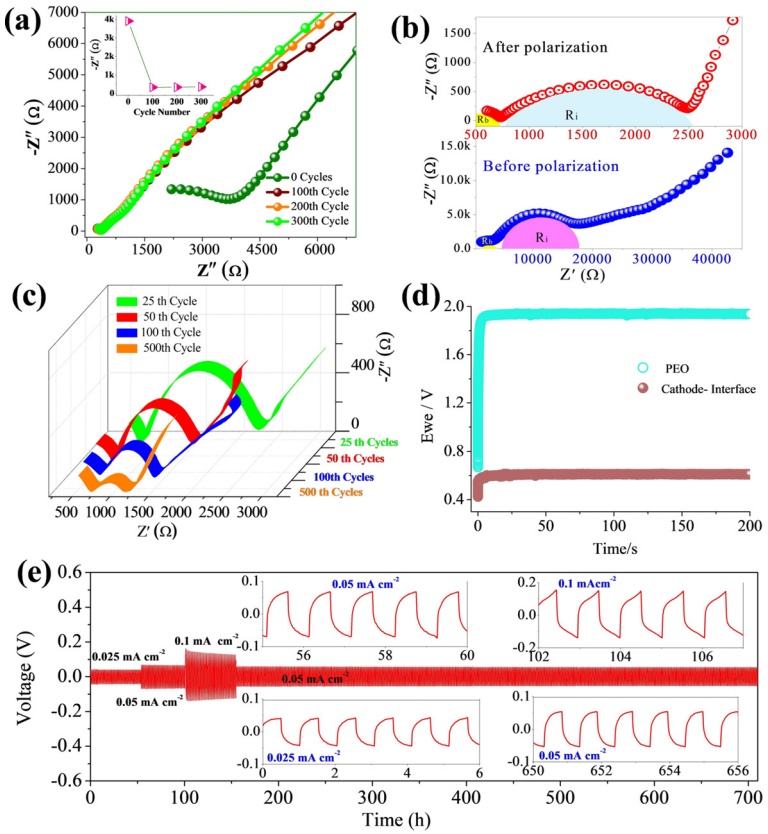

Figure 4. Electrochemical analysis of the interface properties. a) Impedance spectra of the SS || PT-PEO-PT || Li cell cycled at different cycle numbers at 40 °C. b,c) Impedance spectra of the $LiFePO_4$ || PT-PEO-PT || Li cell after and before polarization, with cycle numbers, and at 40 °C. d) Potential–time analysis of polythiophene combined PEO membrane measured by chronopotentiometry based on the principle of a four-point probe at a constant current of 60 nA. e) Voltage profile of lithium plating/stripping on the symmetric Li || PT-PEO-PT || Li cell at different current densities.

0.05 mA cm^{-2}, and only can cycle for about 120 hours along with an erratic voltage profile (Figure S12). Under the same condition, the Li || PT-PEO-PT || Li cell sustained the stable cycling for more than 1100 hours without internal short circuit and hysteresis potential increasing. At higher current density (0.2 mA cm^{-2}), though the increased overpotentials (0.34 V) was observed for Li || PT-PEO-PT || Li, it exhibited steady lithium plating/stripping for consecutive cycle except for the first ten cycles. On the contrary, the Li || PEO || Li cell cannot be cycled continuously due to the high overpotential and unstable interface (Figure S13). The cycling performance with relative low polarization can be ascribed to the in situ formation of stable mixed ionic–electronic transfer interface layer that energetically wets Li surface with electrolyte membrane.[13] The low polarization further indicates a decent ionic–electronic layer that may alleviate the Li^+ concentration gradient and guide homogeneous distribution of electric field at the Li-electrolyte interface.[14]

The all-solid-state cell assembled with $LiFePO_4$ and NCM523 cathodes, Li-metal anode and the PT-PEO-PT membrane were first activated at 60 °C and were tested at 40 °C. As noted in literatures,[15] all-solid-state $LiFePO_4$ || PEO || Li cells generally operate at temperature above 55 °C, ensuring high Li^+ conductivity and rate performance, however, the increasing interface deterioration and internal polarization between electrode and electrolyte would result in rapid capacity fading and poor cycling stability inevitably after long-term charge/discharge cycles. The $LiFePO_4$ || PT-PEO-PT || Li cells can run smoothly at 40 °C due to the stable mixed ionic–electronic transfer layers improve the electrode–electrolyte interface. Figure 5 a,b present charge-discharge curves of the $LiFePO_4$ || PT-PEO-PT || Li at C-rates ranging from 0.1 to 2 C at 40 °C. The cell delivers a high discharge capacity of 162 mAh g^{-1} at 0.1 C, approaching 94.7 % of the theoretical value. As increased the current density, the reversible capacities of $LiFePO_4$ || PT-PEO-PT || Li cell were about 152.6, 137.5, 125.2, 109.9 mAh g^{-1} at C-rate of 0.2, 0.5, 1 and 2 C, respectively, which is much higher than that those previously reported and cycled at temperature above 55 °C (for a detailed comparison see the Supporting Information, Table S1). In view of the cycling stability, $LiFePO_4$ || PT-PEO-PT || Li cells were first investigated at low current density (0.1 C), which could cycle stably over 100 cycles with a capacity retention of ≈ 95 % and a Coulombic efficiency close to 99.8 % (Figure 5 c). At a high charge rate of 2 C, the cell worked smoothly during 1000 charge/discharge cycles, showing very stable specific discharge capacities of ranging from 103 to 109 mAh g^{-1} after initial 10 cycles and high Coulombic efficiency over 99.1 % (Figure 5 d). The stable cycling performance can be attributed to the highly compatible and conductive interface at both electrodes-electrolyte interfaces. At the same time, benefiting from the gradually smaller interface resistance upon charge/discharge cycling (Figure 4 c), the low interfacial barrier allows Li^+ to more easily access the electrode–electrolyte interface.[16] Figure 5 e illustrates the discharge profiles of the $LiFePO_4$ || PT-PEO-PT || Li cell for different cycle numbers at 2 C, the distance between the charge voltage platform and the discharge voltage platform presents a slight decreased trend (Figure S14), which indicates high cycling ability with improving polarization behavior inside the cell.[17] Considering the improved interfacial properties, the $LiFePO_4$ || PT-PEO-PT || Li cell was also examined at 0.05 C under room temperature, and the electrochemical stability of ionic–electronic transfer layer was used to evaluated by high-voltage NCM523 || PT-PEO-PT || Li cell.

The smooth charge-discharge profiles and cycle performance of two cells at low C-rate are exhibited in Figure 5 f,g, which illustrates that the mixed ionic–electronic transfer interface layers have the ability to maintain the superior interface stability and contribute to superior electrochemical performance.

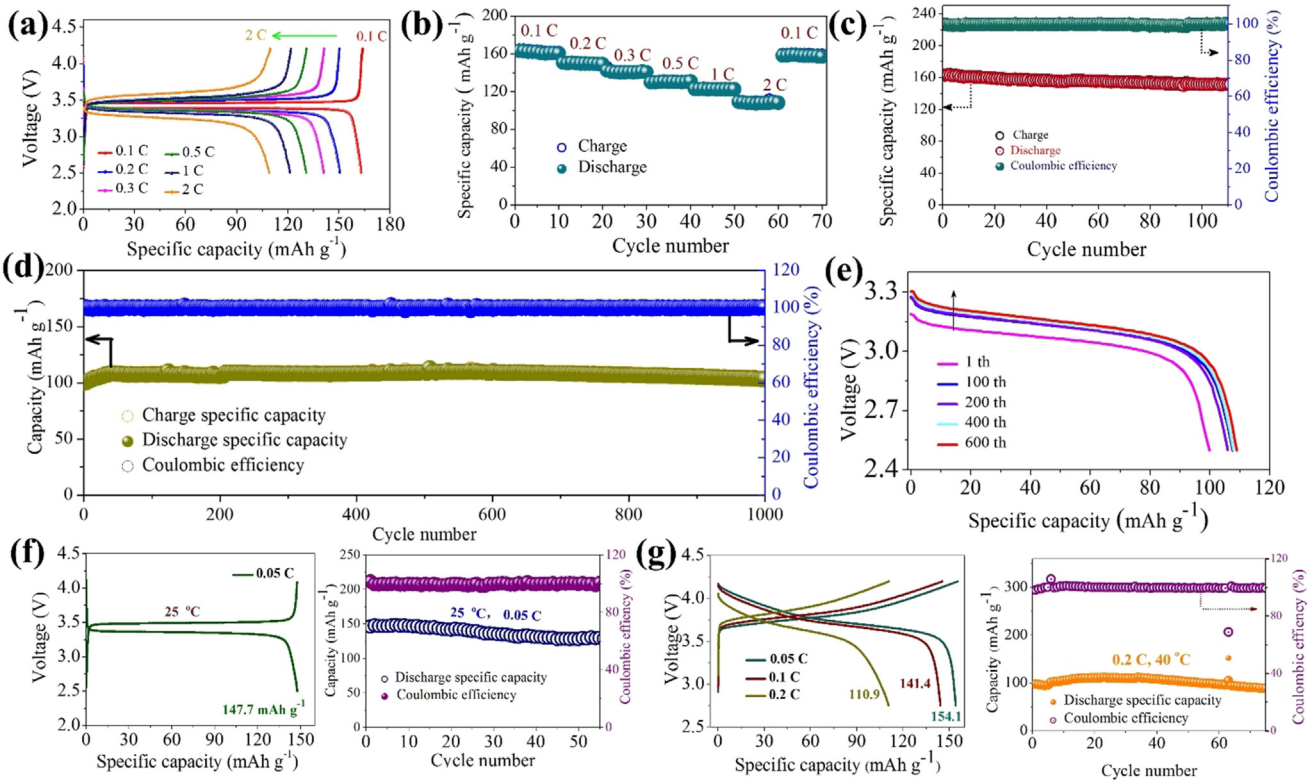

Figure 5. Electrochemical performance of the $LiFePO_4$ || PT-PEO-PT || Li cell after polarization at 40 °C. a) Galvanostatic discharge–charge curves of the cell cycled at various C-rates from 0.1 C to 2 C. b) Rate capability of the cell. c) Cycling performance at 0.1 C. d) Long-term cycling of the cell cycled at 2 C. e) Discharge profiles of the cell for different cycle numbers at 2 C. f) Galvanostatic discharge–charge curves and cycling performance of the cell cycled at 0.05 C and 25 °C. g) Galvanostatic discharge–charge curves and cycling performance of the NCM523 || PT-PEO-PT || Li cell cycled at different C-rates and 40 °C.

Conclusion

We have demonstrated a strategy to significantly solve the interfacial issues of solid-state polymer lithium batteries by introducing in situ conductive polymer layers at both electrode–electrolyte contact areas. After the polythiophene grew from the raw electrolyte at the electrode–electrolyte interface, low interface resistance and highly stable contact between the electrodes and the electrolyte membrane were achieved by introduction of the conductive layer. Further exploring the effect on $LiFePO_4$ || PT-PEO-PT || Li cell performance displayed high discharge capacity and ultralong-term cycling stability at 2 C and 40 °C, demonstrating that the polythiophene layer has the ability to withstand interface degradation and maintain the Li anode–electrolyte interface compatibility and excellent electrical properties. The design strategy, with its simplicity and operability, can be extended to various organic additives, such as pyrrole or thiophene derivatives that are polymerized by an electrochemical method. The conductive polymer interface layer is a promising technology to tackle the solid-solid interface issues in all-solid-state lithium batteries.

Acknowledgements

The authors gratefully acknowledge the financial support provided by the National Natural Science Foundation of China (11972178, 51872131 and 51972156), the Talent Project of Revitalizing LiaoNing (XLYC1807114) and Technology Liaoning Project Grants (2019LNZD01, 2020LNQN17 and 2019QN07).

Conflict of Interest

The authors declare no conflict of interest.

Keywords: lithium-metal batteries · mixed ion-electron interface layers · polymer electrolytes · solid electrolyte interphase · solid-state batteries

[1] a) Y. Gao, D. Wang, Y. C. Li, Z. Yu, T. E. Mallouk, D. Wang, *Angew. Chem. Int. Ed.* **2018**, *57*, 13608 – 13612; *Angew. Chem.* **2018**, *130*, 13796 – 13800; b) J. Wang, Y. Yamada, K. Sodeyama, E. Watanabe, K. Takada, Y. Tateyama, A. Yamada, *Nat. Energy* **2018**, *3*, 22 – 29.

[2] a) Q. Zhou, J. Ma, S. Dong, X. Li, G. Cui, *Adv. Mater.* **2019**, *31*, 1902029; b) N.-W. Li, Y. Shi, Y.-X. Yin, X.-X. Zeng, J.-Y. Li, C.-J.

Li, L.-J. Wan, R. Wen, Y.-G. Guo, *Angew. Chem. Int. Ed.* **2018**, *57*, 1505 – 1509; *Angew. Chem.* **2018**, *130*, 1521 – 1525.
[3] a) X. Yu, A. Manthiram, *Energy Environ. Sci.* **2018**, *11*, 527 – 543; b) W. D. Richards, L. J. Miara, Y. Wang, J. C. Kim, G. Ceder, *Chem. Mater.* **2016**, *28*, 266 – 273; c) N. Wu, P.-H. Chien, Y. Qian, Y. Li, H. Xu, N. S. Grundish, B. Xu, H. Jin, Y.-Y. Hu, G. Yu, J. B. Goodenough, *Angew. Chem. Int. Ed.* **2020**, *59*, 4131 – 4137; *Angew. Chem.* **2020**, *132*, 4160 – 4166.
[4] a) Y. Li, B. Xu, H. Xu, H. Duan, X. Lü, S. Xin, W. Zhou, L. Xue, G. Fu, A. Manthiram, J. B. Goodenough, *Angew. Chem. Int. Ed.* **2017**, *56*, 753 – 756; *Angew. Chem.* **2017**, *129*, 771 – 774; b) X. C. Chen, X. Liu, A. S. Pandian, K. Lou, F. M. Delnick, N. J. Dudney, *ACS Energy Lett.* **2019**, *4*, 1080 – 1085.
[5] a) H. Xu, Y. Li, A. Zhou, N. Wu, S. Xin, Z. Li, J. B. Goodenough, *Nano Lett.* **2018**, *18*, 7414 – 7418; b) B. Wang, Y. Zhao, M. N. Banis, Q. Sun, K. R. Adair, R. Li, T.-K. Sham, X. Sun, *ACS Appl. Mater. Interfaces* **2018**, *10*, 1654 – 1661; c) X. Li, J. Liu, M. N. Banis, A. Lushington, R. Li, M. Cai, X. Sun, *Energy Environ. Sci.* **2014**, *7*, 768 – 778.
[6] a) J. Wen, Y. Huang, J. Duan, Y. Wu, W. Luo, L. Zhou, C. Hu, L. Huang, X. Zheng, W. Yang, Z. Wen, Y. Huang, *ACS Nano* **2019**, *13*, 14549 – 14556; b) G. V. Alexander, N. C. Rosero-Navarro, A. Miura, K. Tadanaga, R. Murugan, *J. Mater. Chem. A* **2018**, *6*, 21018 – 21028; c) Q. Zhao, X. Liu, S. Stalin, K. Khan, L. A. Archer, *Nat. Energy* **2019**, *4*, 365 – 373.
[7] a) Y. Chen, K. Wen, T. Chen, X. Zhang, M. Armand, S. Chen, *Energy Storage Mater.* **2020**, *31*, 401 – 443; b) S. Mu, W. Huang, W. Sun, N. Zhao, M. Jia, Z. Bi, X. Guo, *J. Energy Chem.* **2021**, *60*, 162 – 168.
[8] a) X. Yu, A. Manthiram, *ACS Appl. Energy Mater.* **2020**, *3*, 2916 – 2924; b) D. Dong, B. Zhou, Y. Sun, H. Zhang, G. Zhong, Q. Dong, F. Fu, H. Qian, Z. Lin, D. Lu, Y. Shen, J. Wu, L. Chen, H. Chen, *Nano Lett.* **2019**, *19*, 2343 – 2439.
[9] S. S. Zhang, K. Xu, T. R. Jow, *Electrochim. Acta* **2004**, *49*, 1057 – 1061.
[10] K. Yamamoto, Y. Iriyama, T. Asaka, T. Hirayama, H. Fujita, K. Nonaka, K. Miyahara, Y. Sugita, Z. Ogumi, *Electrochem. Commun.* **2012**, *20*, 113 – 116.
[11] a) H. Zhang, L. Hu, J. Tu, S. Jiao, *Electrochim. Acta* **2014**, *120*, 122 – 127; b) C. Zhang, Y. He, P. Mu, X. Wang, Q. He, Y. Chen, J. Zeng, F. Wang, Y. Xu, J.-X. Jiang, *Adv. Funct. Mater.* **2018**, *28*, 1705432.
[12] a) M. Cai, Y. Lu, J. Su, Y. Ruan, C. Chen, B. V. R. Chowdari, Z. Wen, *ACS Appl. Mater. Interfaces* **2019**, *11*, 35030 – 35038; b) D. Luo, L. Zheng, Z. Zhang, M. Li, Z. Chen, R. Cui, Y. Shen, G. Li, R. Feng, S. Zhang, G. Jiang, L. Chen, A. Yu, X. Wang, *Nat. Commun.* **2021**, *12*, 186.
[13] a) X. Fan, X. Ji, F. Han, J. Yue, J. Chen, L. Chen, T. Deng, J. Jiang, C. Wang, *Sci. Adv.* **2018**, *4*, eaau9245; b) X. Han, Y. Gong, K. Fu, X. He, G. T. Hitz, J. Dai, A. Pearse, B. Liu, H. Wang, G. Rubloff, Y. Mo, V. Thangadurai, E. D. Wachsman, L. Hu, *Nat. Mater.* **2017**, *16*, 572 – 579.
[14] a) H. Huo, Y. Chen, R. Li, N. Zhao, J. Luo, J. G. P. da Silva, R. Mücke, P. Kaghazchi, X. Guo, X. Sun, *Energy Environ. Sci.* **2020**, *13*, 127 – 134; b) Z. Tu, S. Choudhury, M. J. Zachman, S. Wei, K. Zhang, L. F. Kourkoutis, L. A. Archer, *Joule* **2017**, *1*, 394 – 406.
[15] a) Q. Zhang, K. Liu, F. Ding, X. Liu, *Nano Res.* **2017**, *10*, 4139 – 4174; b) H. Xu, P.-H. Chien, J. Shi, Y. Li, N. Wu, Y. Liu, Y.-Y. Hu, J. B. Goodenough, *Proc. Natl. Acad. Sci. USA* **2019**, *116*, 18815 – 18821.
[16] a) B. Sun, C. Xu, J. Mindemark, T. Gustafsson, K. Edström, D. Brandell, *J. Mater. Chem. A* **2015**, *3*, 13994 – 14000; b) C. Yu, S. Ganapathy, E. R. H. van Eck, H. Wang, S. Basak, Z. Li, M. Wagemaker, *Nat. Commun.* **2017**, *8*, 1086.
[17] a) Y. Wang, Y. Wang, E. Hosono, K. Wang, H. Zhou, *Angew. Chem. Int. Ed.* **2008**, *47*, 7461 – 7465; *Angew. Chem.* **2008**, *120*, 7571 – 7575; b) S.-S. Chi, Y. Liu, N. Zhao, X. Guo, C.-W. Nan, L.-Z. Fan, *Energy Storage Mater.* **2019**, *17*, 309 – 316.

Manuscript received: March 24, 2021
Revised manuscript received: May 19, 2021
Accepted manuscript online: May 20, 2021
Version of record online: July 13, 2021

